Journal of Alloys and Compounds 504 (2010) 446–451

Contents lists available at ScienceDirect

Journal of Alloys and Compounds

journal homepage: www.elsevier.com/locate/jallcom

X-ray diffraction and Raman spectroscopy on $Gd_2(Ti_{2-y}Te_y)O_7$ prepared at high pressure and high temperature

A.R. Heredia [a], M. Quintana García [b], J.L. Pérez Mazariego [b], R. Escamilla [a,*]

[a] Instituto de Investigaciones en Materiales, Universidad Nacional Autónoma de México, A. Postal 70-360, México D.F. 04510, Mexico
[b] Facultad de Ciencias, Universidad Nacional Autónoma de México, A. Postal 70-360, México D.F. 04510, Mexico

ARTICLE INFO

Article history:
Received 18 September 2009
Received in revised form 26 May 2010
Accepted 29 May 2010
Available online 11 June 2010

PACS:
72.80.Ng
79.60.Ht
07.35.1k
61.10.–i
87.64.Je

Keywords:
Pyrochlores
$Gd_2Ti_2O_7$
High-pressure synthesis
X-ray diffraction
Raman spectroscopy

ABSTRACT

A series of Te-substituted pyrochlores of stoichiometry $Gd_2(Ti_{2-y}Te_y)O_7$ ($y \leq 0.2$) were prepared under high-pressure and high-temperature conditions and characterized by X-ray diffraction, X-ray photoelectron spectroscopy and Raman spectroscopy. X-ray diffraction and X-ray photoelectron spectroscopy studies revealed that the Te^{4+} and Te^{6+} ions occupy the Ti^{4+}sites; the percentage of the contribution of Te^{6+} increases as tellurium content. These substitutions induce an increase of the volume of the TiO_6 octahedron due to the increase in the Ti–O(2) bond length, which preserves the oxygen positional parameter (x_{48f}) and the Gd–O(1) bond length. Results of Raman spectroscopy showed a significant shift to higher frequencies of the E_g mode associated to the O(2) sublattice, as well an increase in the full-width-at-half-maximum intensity (FWHM) of the F_{2g} mode (O–Gd–O bending) as the level of Te substitution for Ti increases. These results are discussed and compared with those reported in the literature.

1. Introduction

Rare earth (RE) pyrochlore materials of the type $A_2B_2O_7$, where A stands for RE and B for a transition metal, have attracted considerable attention in basic science and engineering. As discovered recently, the tetrahedral geometry of cations in pyrochlore exhibits interesting quantum phenomena at low temperature, such as spin ice [1–3] and quantum liquid [4] states. Applications arise, for example, as candidate for radioactive waste disposal and nuclear engineering [5] and potential electrolytes in solid-oxide fuel cells in pyrochlore compounds with intrinsic ionic conduction [6]. The crystal structure of pyrochlores has been described in different ways by many authors [7–10]. Most of these descriptions consider the coordination polyhedra around the A and B cations: the atomic arrangement is completely specified except for the x positional parameter for the *48f* oxygen site, which defines the displacement from the ideal fluorite structure. There is no displacement at its minimum value at $x = 0.375$, whereas for $x = 0.4375$, its maximum value, the *48f* site is displaced toward the vacant *8b* site. The phase transition between pyrochlore and defect fluorite structure is driven by the coupled anion occupancy of the *8b* site, which results in a seventh oxygen atom coordinating the B cation, and the creation of an anion vacancy on the *8a* site, resulting in an oxygen deficiency coordination of the A cation [11]. The systematic disordering of both the cation and anion sublattices with increasing x has also been confirmed by neutron scattering studies of the closely related pyrochlores, $Y_2(Ti_{1-y}Zr_y)_2O_7$ [12,13] and $Gd_2(Ti_{1-y}Zr_y)_2O_7$ [14,15].

Studies of $A_2B_2O_7$ pyrochlores doped with Te ions have shown that these enter into the structure in either the A sublattice (adopting the oxidation state Te^{4+}) or in the B sublattice (adopting the oxidation state Te^{6+}) [7]. However, the substitution of Te^{4+} ions fully or partially occupying the B sublattice also has been reported [16–18].

Vibrational spectroscopy is ideally suited for the study of crystalline-to-amorphous transitions since there is no requirement for lattice periodicity, unlike diffraction-based techniques. Symmetry analysis of cubic phases such as pyrochlore and fluorite structures, requires that the Raman active and infrared active vibrational modes be mutually exclusive, so several studies of order–disorder transitions in the pyrochlore system have utilized Raman and infrared spectroscopy [19–22].

* Corresponding author.
E-mail address: rauleg@servidor.unam.mx (R. Escamilla).

0925-8388/$ – see front matter © 2010 Elsevier B.V. All rights reserved.
doi:10.1016/j.jallcom.2010.05.143

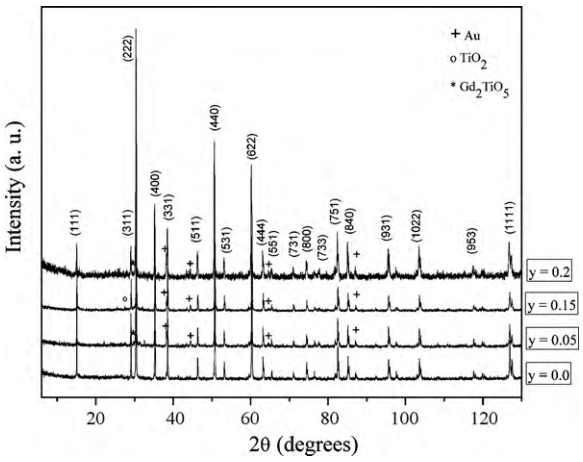

Fig. 1. X-ray diffraction patterns of the $Gd_2(Ti_{2-y}Te_y)O_7$ samples.

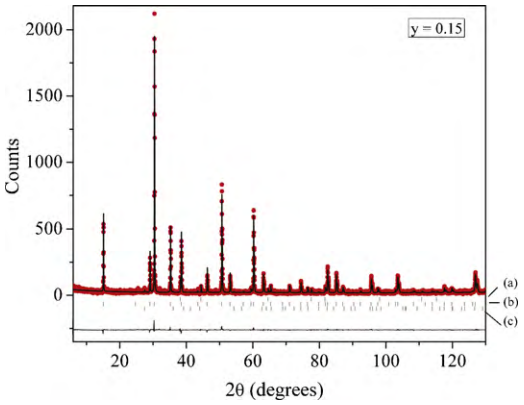

Fig. 2. Rietveld refinement of the X-ray diffraction pattern for $y = 0.15$ sample. Experimental spectrum (dots), calculated pattern (continuous line), their difference (bottom) and the calculated peak positions (middle line). (a) Au, (b) $Gd_2(Ti_{1.85}Te_{0.15})O_7$ and (c) TiO_2 rutile.

In this paper, we describe the Te effect on the crystal structure, the chemical state of Te ions and vibrational modes of pyrochlores of stoichiometry $Gd_2(Ti_{2-y}Te_y)O_7$ ($y \leq 0.2$). The samples were characterized by X-ray diffraction (XRD), X-ray photoelectron spectroscopy (XPS) and Raman spectroscopy.

2. Experimental

Polycrystalline samples of $Gd_2(Ti_{2-y}Te_y)O_7$, with $y = 0$, 0.05, 0.15 and 0.2, were synthesized from starting corresponding oxides, TeO_2, Gd_2O_3 and TiO_2 (99.99% purity) mixed in stoichiometric amounts, sealed in a gold capsule and heated at 900 °C under pressure of 2.1 GPa using a Quickpress piston cylinder press. Phase identification of the samples was done with an X-ray diffractometer Siemens D5000 using Cu K_α radiation and a Ni filter. Intensities were measured at room temperature in steps of 0.02°, in the 2θ range 6–130°. The crystallographic phases were identified by comparison with the X-ray patterns of the JCPDS database. The crystallographic parameters were refined using a Rietveld-fit program, Rietica v 1.71 with multi-phase capability [23].

The chemical analysis was carried out by X-ray photoelectron spectroscopy (XPS). This analysis was performed using a VG Microtech ESCA2000 Multilab UHV system, with an Al K_α X-ray source ($h\nu = 1486.6$ eV), operated at 15 kV and 20 mA beam, and a CLAM4 MCD analyzer. The surface of the pellets was etched for 20 min with 4.5 kV Ar^+ at 0.33 μA mm^{-2}. The XPS spectrum was obtained at 55° to the normal surface in the constant pass energy mode (CAE), $E_0 = 20$ eV for high resolution narrow scan. The peak positions were referenced to the background silver $3d_{5/2}$ photopeak at 368.21 eV, having a FWHM of 1.00 eV, and C 1s hydrocarbon groups in 284.50 eV central peak position. The XPS spectra were fitted with the program SDP v 4.1 [24].

Raman-scattering measurements were performed with a triple Horiba Jobin Yvon T64000 spectrometer equipped with an optical microscope and a photomultiplier tube in a back scattering geometry. A 100× objective was adopted to focus the laser beam of an argon laser (514.5 nm) with a power of 10 mW. Different areas of the samples were measured in order to ensure sample homogeneity. Convolution of the observed bands was done with a Lorentz oscillator model. Fitted curves showed less than 1% error with the corresponding spectra.

3. Results and discussion

3.1. XRD analysis

Fig. 1 shows the powder X-ray diffraction patterns obtained for the system $Gd_2(Ti_{2-y}Te_y)O_7$ type pyrochlore with $y = 0$, 0.05, 0.15 and 0.2. The analysis of these data indicates that the crystal structure of the samples corresponds to $Gd_2Ti_2O_7$ (ICDD no. 73-1698) pyrochlore common structure, although light traces of Gd_2TiO_5 (ICDD no. 21-0342) are observed for the compositions $y = 0.05$ and 0.2, whereas only light traces of TiO_2 (ICDD no. 21-1276) is observed for the sample with $y = 0.15$. Additionally, light traces of Au (ICDD no. 4-0784) are observed in all samples due to the process of synthesis. Mori et al. [25] have shown that the presence of Gd_2TiO_5 or TiO_2 in the pyrochlore $Gd_2Ti_2O_7$ is associated to the effect of vacancies or excess of Gd^{3+} ions in the *16d* sites, respectively.

The X-ray diffraction patterns of the $Gd_2(Ti_{2-y}Te_y)O_7$ samples were Rietveld-fitted using a space group $Fd\bar{3}m$ (No. 227). In the structural refinement we consider the presence of secondary phases and the substitution of Te ions in Ti sites. Fig. 2 shows, as an example, a fitted pattern for $y = 0.15$. Detailed results of the structural refinements are listed in Table 1. In the first two rows we present the evolution of the lattice parameter at room temperature for the $Gd_2(Ti_{2-y}Te_y)O_7$ samples, as function of Te content. It seems that as y is increased, the lattice parameter increases. Fig. 3 shows the evolution of the lattice parameter for the $Gd_2(Ti_{2-y}Te_y)O_7$ samples as a function of Te content (y). For $y = 0$, the lattice parameter was $a = 10.1840(1)$, which is in good agreement with the reported data for $Gd_2Ti_2O_7$ [7].

The increase in the lattice parameter as a function of Te content (y) may be explained considering the coordination number and the ionic radii of the Ti^{4+} and Te^{4+} ions with coordination number 6, in the case of Ti^{4+} the ionic radii is 0.605 Å while that the Te^{4+} is 0.97 Å [26]. From these values, apparently the increase of the unit cell volume may be related to the increase of Te^{4+}, however we cannot discard the possibility of having Te^{6+} in the Ti sites.

Unlike of the substitution of Te ions in the Ti sites, we observed that substituting the Te ions in the Gd sites, in the Rietveld refinement process does not induce significant changes in the quality fitting value of χ^2, therefore we cannot discard this possibility. However, substitution studies with Te^{4+} in the Tl and Te^{6+} in the

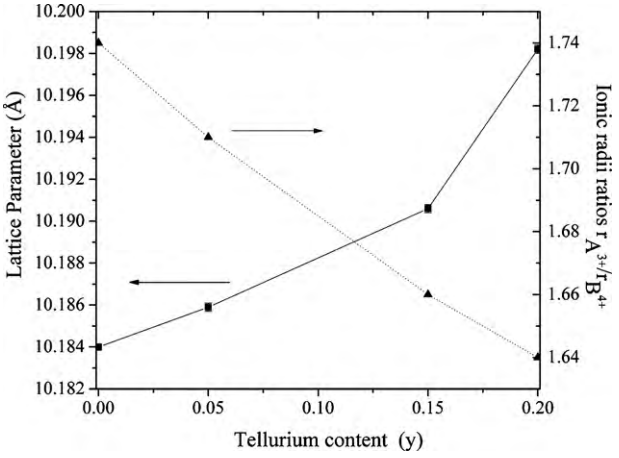

Fig. 3. Crystal lattice parameters and unit cell volume as a function of tellurium content (y).

Table 1
Structural parameters, bond lengths (Å) and bond angles (°) for $Gd_2Ti_{2-y}Te_yO_7$ at 295 K.

	y =		0.0	0.05	0.15	0.20
	a (Å)		10.1840(1)	10.1859(2)	10.1906(2)	10.1982(2)
	V (Å^3)		1056.22	1056.81	1058.28	1060.65
Gd		B (Å^2)	0.17(2)	0.34(2)	0.37(3)	0.67(3)
		N	0.99(2)	0.99(2)	0.99(2)	0.99(1)
(Ti/Te)		B (Å^2)	0.21(8)	0.21(7)	0.28(2)	0.36(9)
O(1)		B (Å^2)	0.7(8)	0.9(4)	1.1(4)	1.2(9)
		N	1.00(4)	0.9(4)	0.99(1)	0.96(1)
O(2)		B (Å^2)	0.6(4)	0.7(3)	0.8(5)	0.8(5)
		N	1.00(2)	1.00(2)	1.00(3)	1.00(3)
		Pos. *x 48f*	0.4319(2)	0.4318(3)	0.4316(3)	0.4313(3)
Bond length (Å)		Gd–O(1): 2	2.205(2)	2.206(2)	2.206(1)	2.208(1)
		Gd–O(2): 6	2.584(4)	2.583(5)	2.582(4)	2.580(4)
		Ti/Te–O(2): 6	1.930(2)	1.930(2)	1.932(1)	1.934(1)
Bond angle (°)		Gd–O(1)–Gd	109.47(2)	109.47(2)	109.47(2)	109.47(2)
		Gd–O(2)–Gd	88.36(4)	88.39(4)	88.46(5)	88.55(5)
		Ti/Te–O(2)–Ti/Te	137.86(3)	137.81(3)	137.69(4)	137.53(4)
		O(2)–Ti/Te–O(2)	92.24(3)	92.27(4)	92.35(4)	92.47(5)
%Gd_2TiO_5			–	2.1(1)	–	2.1(1)
%TiO_2			–	–	1.7(2)	–
Ionic radii ratios r_A/r_B			1.74	1.71	1.66	1.64
R_{wp} (%)			19.1	19.1	20.8	22.8
R_p (%)			15.1	14.5	15.8	17.9
R_{exp} (%)			16.6	17.1	16.8	18.9
χ^2			1.1	1.1	1.5	1.4

Note: Space group: $Fd\bar{3}m$ (No. 227). Atomic positions: Gd: *16c* (0, 0, 0); Ti: *16d* (1/2, 1/2, 1/2); O(1): *8a* (1/8, 1/8, 1/8); O(2): *48f* (x, 1/8, 1/8) position; N is the occupancy factor. % of impurity in the phase.

Mn sites on the $Tl_2Mn_2O_7$ pyrochlore, have found that Te does not enter in the Tl site [18].

As a consequence of the substitution of Te ions in the Ti sites, the oxygen positional parameter (x_{48f}) changes from 0.4319 (y = 0.0) to 0.4313 (y = 0.20). A similar trend has been found upon substitution of Ti by Zr [12–14].

In order to determine the tellurium content that forms a highly ordered pyrochlore it must be considered that the stability of the $A_2^{3+}B_2^{4+}O_7$ pyrochlores is governed by the ionic radii ratio of the A and B site cations (r_A/r_B). For pyrochlores prepared at atmospheric pressure and temperatures up to 1500 °C, the range of pyrochlore stability extends from r_A/r_B = 1.46 for $Gd_2Zr_2O_7$ to r_A/r_B = 1.78 for $Sm_2Ti_2O_7$ [7]. In this context, we calculated the ionic radii ratio r_A/r_B for the concentrations studied with A: Gd^{3+} and B: ($Ti_{2-y}^{4+}Te_y^{4+}$), the results shown a linear behavior from y = 0.0 to 0.2.

In order to establish the effect of Te content we calculated bond lengths and bond angles of the $Gd_2Ti_2O_7$ structure. The Ti^{4+} is located at the center of the corner-sharing oxygen octahedra and form the three-dimensional Ti_2O_6 network, which surrounds the one-dimensional hexagonal chain along the [1 1 1] direction. Although the $Gd_2O(1)$ chains occupy these holes, they only interact weakly with the more rigid Ti_2O_6 network. Our results of the Rietveld-fit shows that the bond length Ti–O(2) increases from 1.930(2) to 1.934(1) Å as the tellurium content augment. The second cation in this structure, Gd^{3+}, is surrounded by eight oxygen atoms in a compressed scalenohedral geometry with six long Gd–O(2) and two short Gd–O(1) bonds. In special, the Gd^{3+} cations and O(1) anions in this oxide form a three-dimensional network constituted of tetrahedral corner sharing. In those cases, the bond length Gd–O(2) decrease from 2.584(4) to 2.580(4) Å and the bond length Gd–O(1) change from 2.205(2) to 2.208(1) Å, as tellurium content increases.

3.2. XPS measurements

To determine the valence state of the Te ion in the structure, X-ray photoelectron spectroscopy studies at room temperature were performed in the system $Gd_2(Ti_{2-y}Te_y)O_7$ type pyrochlore with y = 0.05, 0.15 and 0.2. Fig. 4 shows the deconvolution of the XPS spectra in the Te $3d_{5/2}$ region for all samples. The detailed shape of the signal is fitted assuming the contribution of four components belonging to two different chemical states of the Te-doped samples. The Te $3d_{5/2}$ peaks were localized at binding energies around of 574.8 and 577.8 eV that might be attributed to TeO_2 and TeO_3, respectively [27,28]. These results are consistent with values obtained from tellurium trioxide (TeO_3) and tellurium dioxide (TeO_2) thin films deposited by rf sputtering [29]. We have observed that the intensity of Te $3d_{5/2}$ peak associated to TeO_3 respect to TeO_2 peak increases as Te content does. Thus, the results of Rietveld

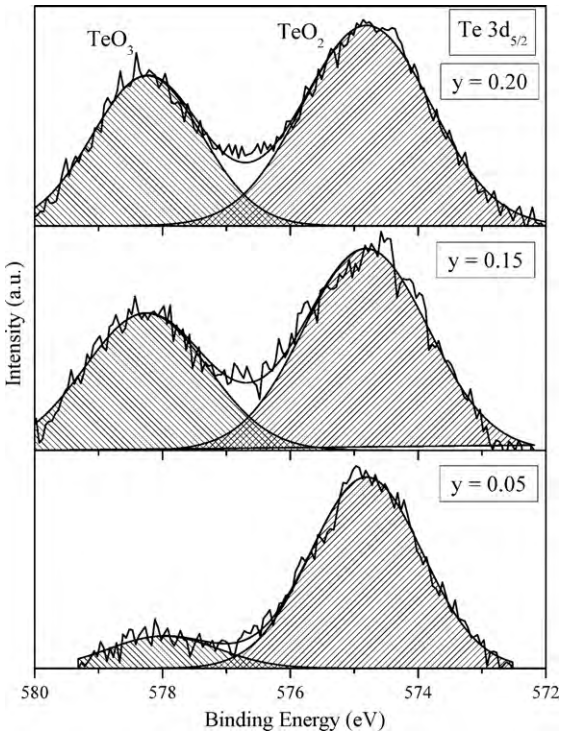

Fig. 4. XPS spectra of Te $3d_{5/2}$ for all samples with Te.

refinement and XPS analysis in this study show that the Te is substituting at the Ti site with mixed valence.

3.3. Raman spectroscopy analysis

Factor group analysis for the cubic rare earth titanate structure ($A_2Ti_2O_7$) of space group $Fd\bar{3}m$ (O_{h7}) indicates that only the normal modes associated to the *48f* and *8a* sites contributes to the Raman spectra, as can be seen from the irreducible representations for each site:

16c site: Ti^{4+} sublattice = $A_{2u} + E_u + 2F_{1u} + F_{2u}$,
16d site: Gd^{3+} sublattice = $A_{2u} + E_u + 2F_{1u} + F_{2u}$,
48f site: O(2) sublattice = $A_{1g}+E_g+2F_{1g}+3F_{2g} + A_{2u}+E_u + 3F_{1u} + 2F_{2u}$,
8a site: O(1) sublattice = $F_{1u} + F_{2g}$.

Thus, excluding the F_{1u} acoustic modes, the decomposition into zone-center normal modes gives the following irreducible representation for the predicted Raman and infrared modes:

$$\Gamma_{opt} := A_{1g}(R) + E_g(R) + 2F_{1g}(I) + 4F_{2g}(R) + 3A_{2u}(ir) + 3Eu(I) + 7F_{1u}(ir) + 4F_{2u}(I).$$
$$\Gamma_{ac} := F_{1u}$$

where *R*, Raman active; ir, infrared active; *I*, inactive; Γ_{opt}, optical modes; Γ_{ac}, acoustic modes.

There are a total of six Raman active modes and seven infrared active modes. Fig. 5 shows the Raman spectra for $Gd_2(Ti_{2-y}Te_y)O_7$ ($y = 0.00$, 0.05, 0.15 and 0.20) and Gd_2TiO_5. The most noticeable features in the Raman spectrum for the $y = 0.0$ sample are the two intense bands localized at ~316 and ~524 cm^{-1}. Also, broad bands appear at ~110, ~210, ~450, and ~700 cm^{-1}. As has been noted in the literature, the first intense band consists of two modes, an F_{2g} mode around 310 cm^{-1} (O–Gd–O bending mode) and an E_g mode around 330 cm^{-1} (O(2) sublattice mode [30,31]). The second intense one, at ~520 cm^{-1}, has been assigned to the A_{1g} mode (Gd–O stretching vibration), which also presents a shoulder on ~560 cm^{-1}. It is observed in all samples a small shift to high frequencies, in a range of 4–6 cm^{-1} depending on the vibrational mode, for all the observed modes as compared with the results in the literature. This might be associated to the synthesis at high pressure and high temperature [15]. For example, the intense bands reported at 310 and 520 cm^{-1} appears in all the spectra at 316 and 524 cm^{-1} respectively. Based on comparison with assignments in previous works on these and related compounds [31,32] the best convolution of the spectrum occurs by fitting with 11 bands. For the

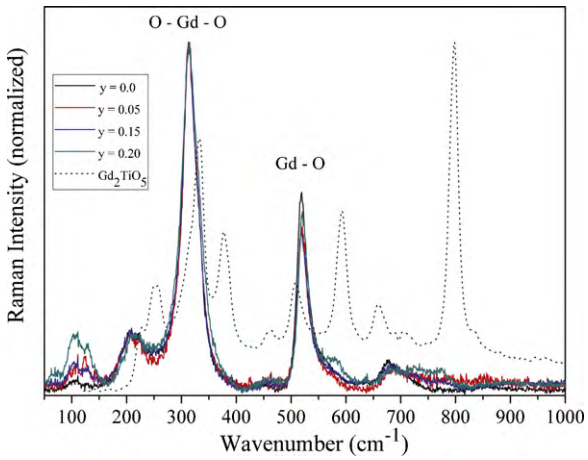

Fig. 5. Raman spectra for the $Gd_2Ti_{2-y}Te_yO_7$ samples and Gd_2TiO_5.

remaining samples ($y = 0.05$, 0.15 and 0.20) the major changes in the spectra occurs in the low frequency region (50–150 cm^{-1}) with subtle changes in the ~450 cm^{-1} region, except for the $y = 0.20$ sample where a broad band around 590 cm^{-1} appears. The assignment of the spectra in this work is made according to that by Maczka et al. [31]. The literature Raman band positions and assignments are summarized in Table 2, along with the observed Raman bands in the spectra of the samples.

The presence of impurities on the samples is difficult to establish from the spectra, since several vibrational frequencies are common to the pyrochlore, the Gd_2TiO_5 (the mode F_{2g} at 331 cm^{-1}) and the TiO_2 rutile type (like the ~450 cm^{-1} band) structures, as can be observed on Fig. 6. Moreover, for the $y = 0.20$ sample, the increase of the band observed at ~587 cm^{-1} can be associated to Gd_2TiO_5, as well for the shoulder in the same wavenumber for the sample $y = 0.05$. Subtracting the Gd_2TiO_5 spectrum from the spectra of both samples gives an estimated value of its presence as 1.8% for the $y = 0.20$ and <1% for the $y = 0.05$ samples. In the case for the sample $y = 0.15$, the presence of TiO_2 rutile is even harder to estimate for impurities less than 5% of the sample. Similar results are observed by Rietveld refinement (see Table 1).

The Raman properties of the Ti-pyrochlore structure mostly arises from the Ti–O(2) network, since the major contribution to the Raman spectrum comes from the O(2) vibration. Therefore, Te doping on Ti sites must change the A_{1g} and E_g modes, associated with the oxygen O(2) vibrations. That seems to be the case for

Table 2
Raman band positions (cm^{-1}) and assignments for the $Gd_2Ti_{2-y}Te_yO_7$ samples and literature values.

Lummen [30] (cm^{-1})		Maczka [31] (cm^{-1})		Sym.	y =			
					0.0	0.05 (cm^{-1})	0.15 (cm^{-1})	0.20 (cm^{-1})
104		–		Accoustic	108 w	109 w	108 w	66 w 105
128		–		Accoustic	–	128 w 147	133	131
205	(F_{2g})	205 (F_{2g} + overtone)		F_{2g}(bending)	213 m	206 m	212 m	215 m
260	(F_{2g})	–			286 w	257	261	256
310	(F_{2g})	312	(F_{2g})	F_{2g}(O–R–O bending)	316 vs	316 vs	316 vs	317 vs
325	(E_g)	330	(E_g)	E_g(O(2) sublattice mode)	332 w	334	336	340
450	(–)	449	(F_{2g})	F_{2g}	454 w	453 w	456 w	444 w
517	(A_{1g})	518	(A_{1g})	A_{1g}(R–O stretching)	523 s	523 s	524 s	526 s
554	(F_{2g})	558	–	–	556 w	538 w	563 w	539
		574 (F_{2g})			–	574 w (and traces of Gd_2TiO_5)	–	576 m 587 w(traces of Gd_2TiO_5)
677		674		2nd order scattering	688 m	686 m	685 m	680 m
(–)		2nd order scattering				704 w	749 w	
703	(–)	–			703 w	700 w	749 m	740 m

w, weak; m, medium; s, strong; vs, very strong.

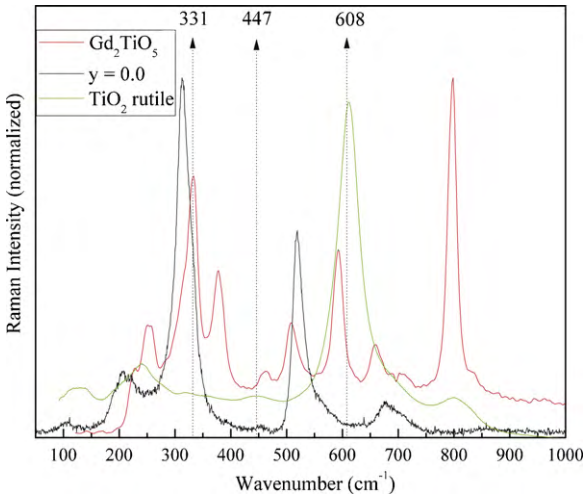

Fig. 6. Comparison of the Gd_2TiO_5 and TiO_2 rutile type with $Gd_2Ti_2O_7$.

the 331 cm^{-1} E_g (O(2) sublattice mode) where a small hardening occurs (~6 cm^{-1}) as Te content (y) augments, as it is shown in Fig. 7. Yet, for the A_{1g} mode (~524 cm^{-1}, Gd–O stretching mode), this figure indicates that it remains almost constant upon doping, as well for the F_{2g} mode at 316 cm^{-1}, associated to the O–Gd–O bending mode. This results clearly indicates that Te doping affects mainly the Ti–O(2) network, and the hardening of the E_g mode should arise from the augmented sublattice parameters, predominantly from the O–O second neighbor interaction.

Fig. 7a and b shows the wavenumber and full-width-at-half-maximum (FWHM) of the E_g (~331 cm^{-1}), A_g (524 cm^{-1}) and the F_{2g} (~316 cm^{-1}) modes in function of Te content (y), respectively. The bandwidth for the A_{1g} mode remains almost constant for the entire substitution series, which indicates that the Gd–O bond stretching is almost unaffected by the substitution. It is the same situation for the E_g mode as it is constant except for the $y = 0.2$ sample, which suffers a significant broadening—even taking into account the error bars arising from the standard deviation of the average of multiple spectra on the same sample, and curve fitting analysis. This broadening must be a consequence of the presence of Gd_2TiO_5 impurity on this sample. It is not the same situation for the F_{2g} mode (O–Gd–O bending vibration) where it broadens monotonically as Te content increases. Since the predominant contribution to the Raman spectra comes from the Ti–O bond stretching, O–Ti–O bond bending, and O–O second neighbor interactions, these results shows that the level of localized short-range disorder is increasing as Te is substituted for Ti. This short-range disorder is most noticeable for the remaining F_{2g} modes, at ~205, ~450, and ~574 cm^{-1}, neither of them present a clear trend upon Ti substitution, and cannot be single out resolved. As has been noted by Maczka et al. [31], polarized Raman experiments on Ti-pyrochlore single crystals shows that there are extra bands at 205, 210, and 650–750 cm^{-1} with A_{1g} symmetry, attributed to second-order transitions, mainly phonon overtones. As can be observed in Fig. 5, the structure in the 200–250 cm^{-1} becomes more complex as Te content increases. This clearly reflects the level of disorder in the structure that yields an increase not only in the coupling of different modes, but also the probability that F_{1u} infrared active phonons, like the one at ~229 cm^{-1} calculated by Gupta et al. [33] (for the Dy pyrochlore), or Raman silent modes, became active. This also holds for the other structures at ~450 and 550–700 cm^{-1}.

Fig. 8 shows the Raman spectra in the 40–200 cm^{-1} region of all the samples. It can be seen for the sample with $y = 0$ that the band at ~109 is very weak and barely resolved. As Te content increases, this band becomes more intense and a band at ~130 cm^{-1} develops. Since these bands are not present on the Raman spectra of single crystals, Maczka et al. [31,32] suggest that their origin comes from the Brillouin zone boundary acoustic modes. According to the data on Table 1, it may be assumed that these bands are related to the breathing mode of the Ti–O(2) (~109 cm^{-1}) and Gd–O(2) (~130 cm^{-1}) networks.

Notably in the pyrochlore-structured samples, the effect of tellurium is clearly evident in the vibrational modes associated with the Gd site. This would suggest that despite their long-range pyrochlore structure, the short-range structure exhibits increasing levels of a localized cation site mixing or fluorite-like disorder. Similar results are observed in the system $Gd_2Ti_{2-y}Zr_yO_7$ [34].

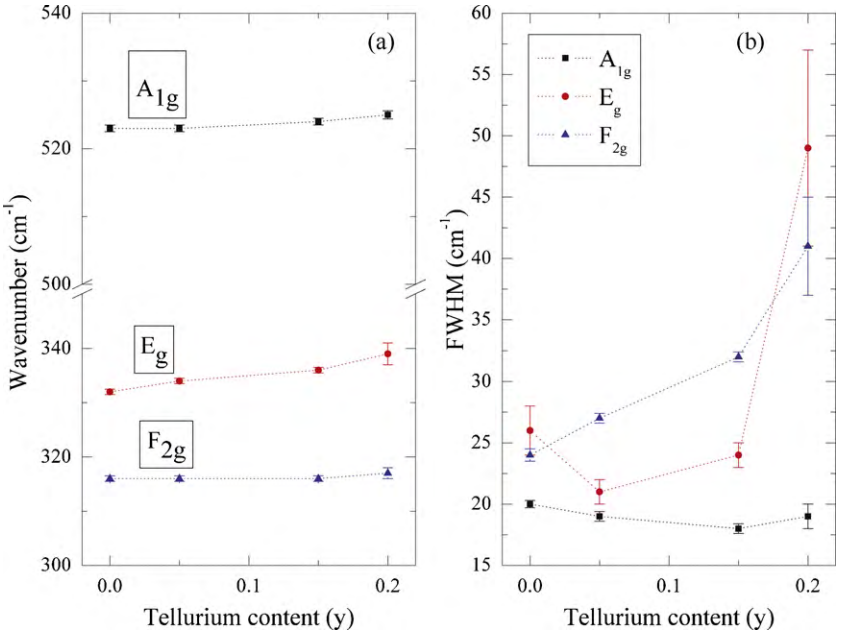

Fig. 7. (a) Raman shift and (b) full-width-at-half-maximum (FWHM) of the E_g, A_g and the F_{2g} modes as a function of tellurium content (y), respectively.

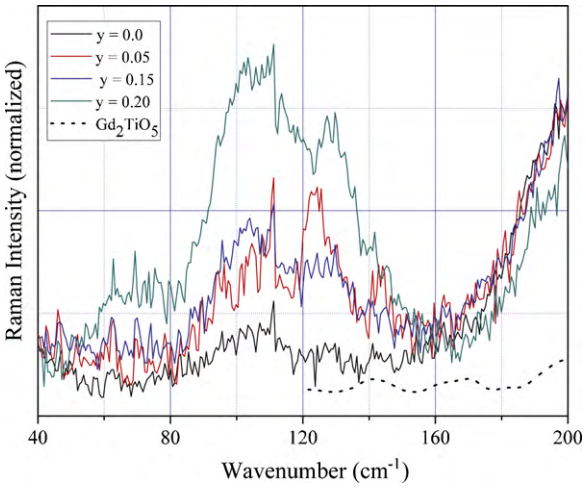

Fig. 8. Raman spectra in the 40–200 cm^{-1} region for all the samples.

4. Conclusions

The $Gd_2Ti_{2-y}Te_yO_7$ pyrochlores with $0 \leq y \leq 0.2$ were synthesized at high pressure and high temperatures. X-ray diffraction Rietveld refinements and X-ray photoelectron spectroscopy studies indicate that tellurium ion occupies the titanium sites with mixed valence (Te^{6+} and Te^{4+}) and the percentage of the contribution of Te^{6+} increases as tellurium content. These substitutions induces an increase of the volume of the TiO_6 octahedron due to the increase in the Ti–O(2) bond length, which preserves the oxygen positional parameter (x_{48f}) and the Gd–O(1) bond length.

Raman spectroscopy measurements also indicate that the level of the short-range disorder in the $Gd_2Ti_{2-y}Te_yO_7$ samples increased as Te was substituted for Ti. The most notable difference in the Raman spectra between the various samples is the coupling of second-order scattering of the Raman active modes and the subtle shift to higher frequencies of the E_g ($\sim$330 cm^{-1}) mode associated to O(2) sublattice and the significant raise in full-width-at-half-maximum intensity (FWHM) of the F_{2g} ($\sim$316 cm^{-1}) mode associated to the O–Gd–O bending vibration, as the Te substitution increases.

Acknowledgments

We thank E. Haro-Poniatowski and M. Picquart from UAM-I for the Raman-scattering measurements. Also to J.A. Diaz and L. Huerta for the XPS measurements. This work was partially supported by projects DGAPA-UNAM IN111408 and IN227208.

References

[1] A.P. Ramirez, A. Hayashi, R.J. Cava, R. Siddharthan, B.S. Shastry, Nature 399 (1999) 333–335.
[2] S.T. Bramwell, S.R. Giblin, S. Calder, R. Aldus, D. Prabhakaran, T. Fenell, Nature 461 (2009) 956–960.
[3] J.E. Greedan, J. Alloys Compd. 408–412 (2006) 444–455.
[4] H.R. Molavian, M.J.P. Gingra, J. Phys.: Condens. Matter 21 (2009) 172201.
[5] Catharina Nästren, Regis Jardin, Joseph Somers, Marcus Walter, Boris Brendebach, J. Solid State Chem. 182 (2009) 1–7.
[6] B.P. Mandal, S.K. Deshpande, A.K. Tyagi, J. Mater. Res. 23 (2008) 911.
[7] M.A. Subramanian, G. Aravamudan, G.V. Subba Rao, Prog. Solid State Chem. 15 (1983) 55–143.
[8] C. Wan, Z. Qu, A. Du, W. Pan, Acta Mater. 57 (2009) 4782–4789.
[9] B.B. Hinojosa, J.C. Nino, A. Asthagiri, Phys. Rev. B 77 (2008) 104123.
[10] M. Uno, A. Kosuga, M. Okui, K. Horisaka, S. Yamanaka, J. Alloys Compd. 400 (2005) 270–275.
[11] N.J. Hess, B.D. Begg, S.D. Conradson, D.E. McCready, P.L. Gassman, W.J. Weber, J. Phys. Chem. B 106 (2002) 4663–4677.
[12] C. Heremans, B.J. Wuensch, J.K. Stalick, E. Prince, J. Solid State Chem. 117 (1995) 108–121.
[13] O. Knop, F. Brisse, L. Castelliz, Can. J. Chem. 47 (1969) 971–990.
[14] P.K. Moon, Electrical conductivity and structural disorder in $Gd_2Ti_2O_7$–Gd_2Zr_2O7 and $Y_2Ti_2O_7$–$Y_2Zr_2O_7$ solid solutions, Ph.D. Thesis, Massachusetts Institute of Technology, Cambridge, MA, 1988.
[15] F.X. Zhang, J. Lian, J.M. Zhang, K.J. Moreno, A.F. Fuentes, Z. Wang, R.C. Ewing, J. Alloys Compd. 494 (2010) 34–39.
[16] F.A. Weber, T. Schleid, Z. Anorg. Allg. Chem. 626 (2000) 1285–1287.
[17] J. Soler, J. Lemus, M.P. Pina, J. Sanz, A. Aguadero, J.A. Alonso, J. New Mater. Electrochem. Syst. 12 (2009) 77–80.
[18] P. Velasco, J.A. Alonso, M.J. Martínez-Lope, M.T. Casais, J.L. Martínez, M.T. Fernández-Díaz, J.M. de Paoli, Phys. Rev. B 64 (2001) 184436.
[19] W.E. Klee, G. Weitz, J. Inorg. Nucl. Chem. 31 (1969) 2367–2372.
[20] B.E. Scheetz, W.B. White, J. Am. Ceram. Soc. 62 (1979) 468–470.
[21] R.A. McCauley, J. Opt. Soc. Am. 63 (1973) 721–725.
[22] J.F. McCaffrey, N.T. McDevitt, C.M. Phillippi, J. Opt. Soc. Am. 61 (1971) 209–212.
[23] C.J. Howard, B.A. Hunter, D.A.J. Swinkels, Rietica, IUCR Powder Diffract. 22 (1997) 21.
[24] SDP v4.1 (32 bit) Copyright© 2004, XPS International, LLC (compiled 17.01.04).
[25] M. Mori, G.M. Tompsett, N.M. Sammes, E. Suda, Y. Takeda, Solid State Ionics 158 (2003) 79–90.
[26] R.D. Shannon, Acta Crystallogr. A 32 (1976) 751–767.
[27] C.D. Wagner, W.M. Riggs, L.E. Davis, J.F. Moulder, J.E. Millenberg, Handbook of the X-ray Photoelectron Spectroscopy, Perkin-Elmer Corporation, Eden Draivie, MN, 1979.
[28] D. Briggs, M.P. Seah, Practical Surface Analysis by Auger and X-ray Photoelectron Spectroscopy, John Wiley, New York, 1983.
[29] N. Dewan, K. Sreenivas, V. Gupta, Sens. Actuator A: Phys. 147 (2008) 115–120.
[30] T.T.A. Lummen, I.P. Handayani, M.C. Donker, D. Fausti, G. Dhalenne, P. Berthet, A. Revcolevschi, P.H.M. van Loosdrecht, Phys. Rev. B 77 (2008) 214310.
[31] M. Maczka, M.L. Sanjuán, A.F. Fuentes, L. Macalik, J. Hanuza, K. Matsuhira, Z. Hiroi, Phys. Rev. B 79 (2009) 214437.
[32] M. Maczka, J. Hanuza, K. Hermanowicz, A.F. Fuentes, K. Matsuhira, Z. Hiroi, J. Raman Spectrosc. 39 (2008) 537.
[33] H.C. Gupta, et al., J. Mol. Struct. 937 (2009) 136–138.
[34] B.D. Begg, N.J. Hess, D.E. McCready, S. Thevuthasan, W.J. Weber, J. Nucl. Mater. 289 (2001) 188–193.